



Optical, Dielectric and Optoelectronic Properties of Spray Deposited Cu-doped Fe₂O₃ Thin Films

A. Y. Fasasi^a, E. Ajenifuja^{a,*}, E. Osagie^{a,d}, L. O. Animasaun^{c,d}, A. E. Adeoye^b, E. I. Obiajunwa^a

^aCentre for Energy Research & Development, Obafemi Awolowo University, Ile-Ife, Nigeria.

^bTechnical University, Km 15, Lagos Ibadan Expressway, Ibadan, Oyo State, Nigeria.

^cDepartment of Physics, Electronics & Earth Sciences, Fountain University, Osogbo, Osun State, Nigeria.

^dPhysics & Engineering Physics Department, Obafemi Awolowo University, Ile-Ife, Nigeria.

Abstract

Copper-doped hematite thin films were prepared by spray pyrolysis technique using a mixture of ethanol and distilled water precursors. Visual observations showed that aqua precursor produced films of less integrity compared with ethanol that produced thin, uniform and transparent yellowish-brown films that adhered well to the substrate. Composition and thickness measurements determined by RBS revealed that ethanol precursor produced thinner films of 94.45 and 51.77 nm while aqua precursor produced films of 1,370 and 1,120 nm for undoped and Cu-doped Fe₂O₃ respectively. This is an indication that ethanol solutions produced nano-thick films of high integrity. The composition revealed that only the Cu-doped Fe₂O₃ deposited by ethanol solution gave composition close to stoichiometric Fe₂O₃ while the others gave non-stoichiometric Fe (OH)₃. Optical characterization carried out using UV-visible spectrophotometer in transmittance mode indicated that the film thickness was directly proportional to the number of passes which is inversely proportional to the transmittance. Three bandgap determination methods namely; Tauc, Absorption Fitting Spectrum (AFS) and Davis-Mott were employed with the result that Tauc and AFS gave close direct and indirect bandgap energies (E_g) of 3.44 and 1.98 for AFS and 3.43 and 2.32 eV for Tauc respectively. The Urbach tail energy determined was 1,100 meV which is an indication of a broad onset of absorption. The steepness parameter (σ) was found to be 7.83 while the electron-phonon (E_{ph}) coupling energy was found to be 0.85 eV. It was also observed that the refractive index (n) was about 15 times greater than the extinction coefficient (k). In the study of the dispersion parameters using single oscillator and Sellmier models, the values of the single oscillator energy (E_{osc}), dispersion energy (E_d), zero frequency dielectric constant (ϵ_0), zero frequency refractive index (n₀), the average oscillator strength (S₀), the average oscillator parameter (λ_0) and the dispersion parameters were determined. All the values of the parameters estimated are of the same order of magnitude with other semiconducting materials. The study showed that Cu-doped Fe₂O₃ could be employed as dielectric material as well as in optoelectronic devices.

DOI:10.46481/jnsps.2023.1180

Keywords: Thin film, bandgap, Urbach energy, refractive index, dispersion parameters, oscillator parameters

Article History :

Received: 07 November 2022

Received in revised form: 13 March 2023

Accepted for publication: 15 March 2023

Published: 14 June 2023

© 2023 The Author(s). Published by the Nigerian Society of Physical Sciences under the terms of the Creative Commons Attribution 4.0 International license (<https://creativecommons.org/licenses/by/4.0>). Further distribution of this work must maintain attribution to the author(s) and the published article's title, journal citation, and DOI.

Communicated by: E. A. Emile

1. Introduction

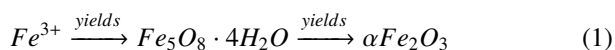
Metal oxides possess a broad range of electrical, chemical, and physical properties that are often highly sensitive to changes in their chemical environment. Because of these

*Corresponding author tel. no: +2348057415551

Email address: eajenifuja@gmail.com (E. Ajenifuja)

properties, metal oxides have been widely studied and specific applications are based on appropriately structured and doped oxides [1]. The enhancement in the gas sensing performance of metal oxides by electron, ultraviolet, and plasma irradiations was due to the modified surface structure [2]. Nanocrystalline transition metal oxide particles and films have found considerable interest in recent years because of their special properties, such as a large surface-to-volume ratio, increased activity, special electronic and unique optical properties, as compared to those of the bulk materials. The oxides of transition metals are an important class of semiconductors, which have applications in magnetic storage media, solar energy transformation, electronics, and catalysis [3]. Magnetic nanoparticles of iron oxide due to their biocompatibility, catalytic activity, and low toxicity have dragged significant attention for their applications in various fields of medical care such as drug delivery systems, cancer therapy, and magnetic resonance imaging. Apart from the biomedical applications, these iron oxide nanoparticles are of technological importance due to their application in many fields including high density magnetic storage devices, ferro-fluids, magnetic refrigeration systems, catalysis, and chemical/ biological sensors [4].

Fe and O form a number of phases, e.g., FeO (wustite), Fe₃O₄ (magnetite), α -Fe₂O₃ (hematite), and γ -Fe₂O₃ (maghemite). The latter phase is synthetic while the remaining oxides occur in nature. The Fe-O phase diagram shows the predominance of the Fe₂O₃ stoichiometry for most temperature and pressure preparation conditions [5, 6]. Of all the transition metal oxides, α -Fe₂O₃ has been extensively studied due to its low cost, high chemical stability, nontoxicity, abundance in nature, and biocompatibility [7]. Hematite crystals are believed to nucleate and grow from iron (III) organic complex which through hydrolytic breakdown yield nano-sized ferrihydrite aggregates that eventually transform to α -Fe₂O₃ through dehydration and rearrangement according to the following equation [8]:



Certain studies believed that without slight deviation from stoichiometry, iron oxide (α -Fe₂O₃) is a thermodynamically stable oxide of the hexagonal packed crystal structure is considered an insulator with localised Fe³⁺ ions while with a slight deviation from stoichiometry hematite is an n-type indirect semiconductor with bandgap energy commonly considered to be 2.2 eV [9]. Some studies have also shown that hematite can exhibit both indirect and direct transitions with indirect and direct bandgap energies around 1.9 and 2.7 eV [4, 7, 10–15]. This range of band gap energy has conferred on hematite the ability to be employed in many electrochemical applications since about 29 % of visible light has energies greater than the hematite band gap (2.2 eV) [16] as a result of which α -Fe₂O₃ is capable of absorbing a large portion of the visible solar spectrum (absorbance edge ~600 nm). With all of these advantages, the usage of α -Fe₂O₃ has been restricted by many anomalies such as higher electron-hole recombination rate leading to poor electrical conductivity with a hole length of 2

– 4 nm, poor mobility, insufficient ionic diffusion rate leading to low specific capacitance and VB positioning (VB is positive with respect to H+/H₂ potential) [9, 17–19].

Several methods have been used to improve on the limitations of α -Fe₂O₃ for improved solar conversion. Enormous efforts were devoted to the modification of the electronic structure of hematite via doping [20], thin film deposition, core-shell structure, and coating. To this end, Sn [21, 22], Ti [20, 29], Si [23, 30], Zn [24], MgO and CaO [26], Ir [27], Zr [31], Cu [32], Ti+Al [25], Ti+Sn [28] –doped and undoped [33, 34] have been employed to dope Fe₂O₃ individually or in combination as photoanodes for water splitting application. On the other hand, Cr [35, 36], Nd [37], ZnO [38], and Eu [39] have been used to dope α -Fe₂O₃ for improving the magnetic properties.

In the area of portable, flexible and wearable electronics and asymmetric supercapacitors undoped α -Fe₂O₃ [40, 41], Carbon incorporated α -Fe₂O₃ on carbon nanotube [18], α -Fe₂O₃/graphene/Ink [42], α -Fe₂O₃ on carbon cloth [43], oxygen vacancy engineered α -Fe₂O₃ nanoarrays on carbon cloth [44], α -Fe₂O₃ nanorods in Ni/Fe battery [45], MXene@ α -Fe₂O₃ coreshell /carbon cloth [46], Si@ α -Fe₂O₃/carbon cloth [47], Polypyrrole doped α -Fe₂O₃ [48], α -Fe₂O₃@PANI core-shell [49], TiO₂@ α -Fe₂O₃ coreshell on array of carbon cloth [50] and Cu-doped α -Fe₂O₃ [51] have all been employed to increase the conductivity of α -Fe₂O₃. For environmental remediation through waste water treatment, α -Fe₂O₃/Ppy for photocatalyst degradation of methylene blue under UV irradiation [52], α -Fe₂O₃ in the treatment of oily waste water [53], pure copper and GO-doped α -Fe₂O₃ [54] for waste water treatment, Cu-doped Fe @Fe₂O₃ coreshell nanoparticles for removing AS(III) for Smelting waste water [55], Zn-doped α -Fe₂O₃ for photocatalytic degradation of Rose Bengal dye [56], activated carbon coated α -Fe₂O₃ adsorbent for chlorinated gas treatment [57], Ni-doped α -Fe₂O₃ for removing toxic metals for aqueous solution [58], Y₂O₃/ α -Fe₂O₃/TiO₂ [59] and α -Fe₂O₃@CeO₂-ZrO₂/Polygorskite [60] composite catalysts for treatment of organic pollutants have all been used successfully. As gas sensors, Pd-doped α -Fe₂O₃ [61], Nb-doped α -Fe₂O₃ [62], Cu-doped α -Fe₂O₃ [63], and Ti- α -Fe₂O₃ [64] have all been synthesised and employed for LPG, NO, NO_x, ethanol and CO gas sensing, respectively.

Different method of synthesis have been used to produce doped α -Fe₂O₃ such as ultrasonic spray pyrolysis [4], DC magnetron and DC pulsed hollow cathode sputtering system [7], SILAR (10), normal spray pyrolysis [16], flame annealing [21], atmospheric pressure CVD [23], Electrodeposition [31], Coprecipitation [36, 64, 69], combustion synthesis method [37], gelation and polymerisation [52], sol-gel [54, 56, 70], high energy ball milling [58], pulsed laser deposition [65], Filtered arc deposition [67], oxygen- plasma assisted MBE [69]. Of all the methods of preparation, spray pyrolysis offers the ease of preparing small as well as large area coating of thin films and nanopowders at low cost for different technological applications. Moreover, it does not require high quality targets nor

vacuum at any stage of preparation. The deposition rate and the film thickness can be controlled effectively by changing the spray parameters such as the precursor composition, nozzle to substrate distance, flow rate, and the number of passes. Most of the studies on Cu-doped α -Fe₂O₃ focussed mainly on the application and not on the detailed optical and dielectric studies needed to determine the areas of applications. This study therefore presents detailed optical and dielectric studies of Cu-doped α -Fe₂O₃ films deposited using spray pyrolysis technique, UV-visible spectrometry and Rutherford backscattering spectroscopy (RBS).

2. Experimental Procedure

The starting solutions were prepared from Iron (III) chloride (FeCl₃) and copper (II) chloride (CuCl₂) purchased from Sigma Aldrich with ethanol and distilled water as solvents. The salts were analytical grade and used as purchased without further purification. For the aqueous solution, 0.1 M solution of iron (III) chloride was prepared by dissolving 4.0 g of FeCl₃ and 2.56 g of CuCl₂ in 250 ml of distilled water. For ethanol solution, the same mass of FeCl₃ was dissolved in 250 ml of ethanol while CuCl₂ was dissolved in a mixture of ethanol: distilled water in the ratio of 200:50 giving four different solutions. The solutions were thoroughly stirred using a magnetic stirrer. The Pyrex glass substrates were cleaned in dilute hydrochloric acid, alcohol, and distilled water and dried in an oven before deposition at a substrate temperature of 320 ± 5 °C and nozzle-to-substrate distance of 23 cm. Suction-based airbrush and air blast atomization was employed for the depositions. For Cu-doped Fe₂O₃ deposition, the FeCl₃:CuCl₂ volume ratio of 80:20 was adopted. After deposition, the samples were annealed in a tubular furnace at different temperatures ranging from 350 -500 °C in air.

The RBS experiment was performed using the 1.7 MeV Pelletron Tandem Accelerator at the Centre for Energy Research & Development, Obafemi Awolowo University, Ile-Ife, Nigeria. For this purpose, 4He²⁺ ion beam was used as projectile ions. The scattering angle was 165° and the resolution of the detector was 12 keV. During the process of acquiring the spectra data, the energy of the ion beam used was 2.2 MeV. All measurements were performed at room temperature with current varying between 20 and 60 nA at a constant charge of 20 μ C. All the spectra were fitted using Windows SIMNRA software for the determination of the composition and the thickness of the films. The optical properties were studied using a Stellanet UV-visible spectrophotometer (Model EP2000) with wavelength covering 200 to 1100 nm in the transmission mode.

3. Results and Discussion

3.1. Visual Observation

Typical surfaces of the deposited films are shown in Figure 1 for doped and undoped films. The surfaces are clean and regular without voids with strong adherence to the substrate. The change in colour due to Cu addition is obvious.



Figure 1: Surfaces of the undoped (left) and Cu-doped (right) Fe₂O₃ deposited films taken by an optical camera Camon 12 Pro.

3.2. RBS Study - Determination of the Thickness and Composition.

Preliminary results of the RBS analyses of the four films grown on Pyrex glass using ethanol and distilled water as solvents for doped and un-doped Fe₂O₃ is presented in Figure 2 (a-d). The shape of the spectra clearly showed the effect of the solvent employed in depositing the films. Sharp peaks are associated with ethanol while broad peaks are associated with distilled water. This may be due to the film thickness and the degree of structural orderliness. All the films deposited using distilled water for the same number of passes are 15 times thicker than the films deposited using ethanol as shown in Table 1. This may also be an indication of the film integrity in that alcohol solutions produced more ordered films than distilled water.

The spraying process employed in this study can lead to the formation of films of FeOH, FeO, Fe₂O₃, or Fe₃O₄. In a pure crystal the ratio of atomic content Fe:O is 0.5:0.5 for FeO, 0.4:0.6 for Fe₂O₃, 0.429:0.571 for Fe₃O₄ and Fe: OH of 0.25:0.75 for Fe(OH)₃. From the elemental composition of the films, we can deduce that the films are neither FeO nor Fe₃O₄. The RBS simulation of the films gave the atomic percentage of Fe, O and Cu. The results, using Fe/O values in Table 1, indicate that undoped alcohol and undoped distilled water precursors produce non-stoichiometric films of Fe(OH)₃ with anion deficiency compensated by excess cation for undoped alcohol precursor and cation vacancies compensated by excess oxygen for undoped aqua precursor.

In the case of Cu-doped precursors, distilled water also produce non-stoichiometric films of Fe(OH)₃ but with Ca substituting for Fe and both anion and cation vacancies are probably compensated by Cu. This explains the high content of Cu in the film but does not explain the incursion of Ca into the film. To explain the presence of Ca in the film, the RBS of the substrates for each film were also analysed simultaneously with the film and the result is shown in Table 2. It is obvious from the table that Ca did not diffuse from the substrate into the film and therefore we may infer that Ca got introduced into the film from the distilled water used as a solvent. But there is no presence of Ca in the undoped aqua precursor and this led us to believe that Cu must have acted as a catalyst in the film formation and coexisted in the film without forming a compound with Fe.

Lastly, for Cu-doped ethanol precursor producing film thickness of 51.77 nm, the Fe/O ratio of the film gave a value of 0.660 which is very close to 0.667 for pure Fe₂O₃. It can then

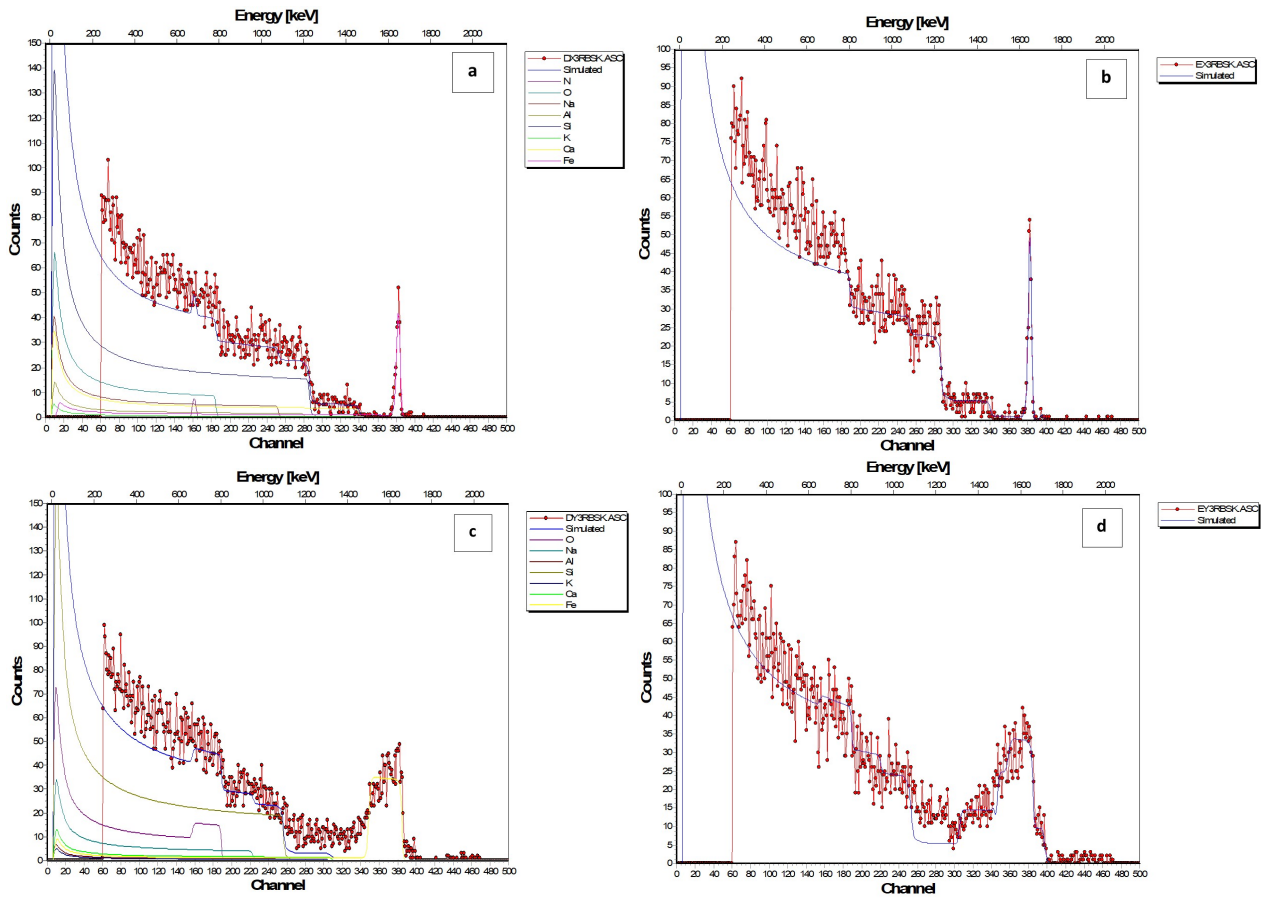


Figure 2: RBS spectral of undoped and Cu-doped Fe_2O_3 in ethanol (a, b) and undoped and Cu-doped Fe_2O_3 in distilled water (c, d).

be said that Cu acted as a catalyst for the formation of Fe_2O_3 and existed in the film as a solid solution without forming a definite phase in the film. Hence, from this point, further analyses will focus solely on Cu-doped alcohol precursors.

3.3. Transmission Analyses

The effect of the number of passes on Cu-doped Fe_2O_3 is depicted in Figure 3a where it can be seen that the increase in the number of passes led to a decrease in transmittance. This trend had been observed in CuO film deposited by spray pyrolysis [71]. Two distinct regions can be observed on the spectra with the line of demarcation around 648 nm which corresponds to 1.92 eV. At this wavelength, the transmittance for 40, 60, and 80 passes were 85, 82, and 78% respectively. Above this wavelength is region 2 where the transmittance is slowly varying as the wavelength increases. Below this wavelength is region 1 where the transmittance is rapidly changing as the wavelength decreases. Region 1 is the absorbing region with 80 passes having the highest absorbance which is probably due to the increased thickness of the film as the number of passes increased while region 2 is the transparent region. This result showed that the film is slightly opaque to photon energies less than 1.92 eV and that it can serve as an optical window and a good solar absorber material. Figure 3b is the comparison of the transmittance of Cu-doped Fe_2O_3 films grown on borosilicate glass with 80 passes using deionized water and alcohol.

The graph shows that deionised water produced thicker film due to the low transmittance (maximum of 30%) while ethanol produced thinner films of high transmittance (maximum of 80%). This corroborates the results obtained from RBS.

3.4. Absorption Coefficient and Skin Depth

3.4.1. Absorption Coefficient

The absorption coefficient α of a semiconducting material is an important parameter useful in determining how the incoming photon energy interacts with the atoms of the semiconductor. The absorption coefficient was calculated using the relation

$$\alpha = \frac{1}{t} \ln \left(\frac{1}{T} \right) \quad (2)$$

Since it is a function of the energy of the incoming photon, Figure 4a depicts the variation of the absorption coefficient with the wavelength of the interacting photon where it can be seen that the absorption is high at high photon energy (ultraviolet region) and decrease gradually till 700 nm where it becomes invariant at the lowest value of $5.0 \times 10^4 \text{ cm}^{-1}$. This trend has been observed in many films even prepared with different methods [72]. The high value of the absorption coefficient makes the material a good absorber and very useful in optoelectronic applications.

Table 1: Thickness (nm) and composition (at. %) of the annealed films from RBS analyses.

Precursor	Thickness	Fe	O	Cu	Ca	Fe:O	Fe/O	Remark
Undoped alcohol Sol ⁿ	94.45 nm	27.83	72.17	-----	-----	0.278 : 0.723	0.359	Fe(OH) ₃
Cu-doped alcohol Sol ⁿ	51.77 nm	39.35	59.62	1.03	-----	0.394 : 0.596	0.660	Fe ₂ O ₃
Undoped aqua Sol ⁿ	1370 nm	17.85	82.15	-----	-----	0.179 : 0.822	0.217	Fe(OH) ₃
Cu-doped aqua Sol ⁿ	1120.80	13.56	69.26	4.40	12.77	0.136 : 0.693	0.196	Fe(OH) ₃

Table 2: Composition (at. %) of the substrate employed for the films

Film	Thickness (nm)	Ca	Si	O	Fe	Na	Al
Fe ₂ O ₃ /alcohol	94.45	1.83	28	56	0.52	12.6	0.53
Cu-Fe ₂ O ₃ /alcohol	51.77	1.83	28	56	0.52	12.6	0.53
Fe ₂ O ₃ /distilled H ₂ O	1370	1.83	28	56	0.52	12.6	0.53
Cu-Fe ₂ O ₃ /distilled H ₂ O	1120.80	1.83	28	56	0.52	12.6	0.53

3.4.2. Skin Depth

On the other hand, when a ray of light passes through thin films, the photon intensity decreases dramatically for many reasons, like the density of the material, refractive index, morphology of the surface, and the film microstructure. The thickness of the film that causes the intensity of the photon to be reduced to $1/e$ value below the surface of the film is called the skin depth δ which is defined as the inverse of the absorption coefficient $\delta = \frac{1}{\alpha}$. It is therefore a function of frequency and hence the band gap. Fig. 4b is depicting the connection between the skin depth and photon energy of Cu-doped Fe₂O₃. The gradual decrease in skin depth can be seen until it gets to a minimum depth of 2.68×10^{-6} cm (26.8 nm) at around 4 eV ($\lambda = 342$ nm). This minimum skin depth of 26.8 nm corresponds to the middle of the film. This result is contrary to other studies where it was shown that the skin depth reduced to zero at a certain energy corresponding to the cut-off wavelength λ_{cutoff} [72, 73]. This may be because the nature of their films was glassy and contain a mixture of crystalline and amorphous phases whereas the film in this study may be completely crystalline.

3.4.3. Bandgap determination

For the photon energy range corresponding to the transmittance spectra, the absorption coefficient can be approximated by simple expressions. For example, assuming a parabolic E versus k relationship, the absorption in semiconductors and dielectrics films can be expressed as

$$\alpha = \frac{B(h\nu - E_g)^m}{h\nu} \text{ for } h\nu > E_g \quad (3)$$

The quantity α is the absorption coefficient, $h\nu$ denotes photon energy, B is a constant that includes information of the convolution of the valence and conduction band states and on

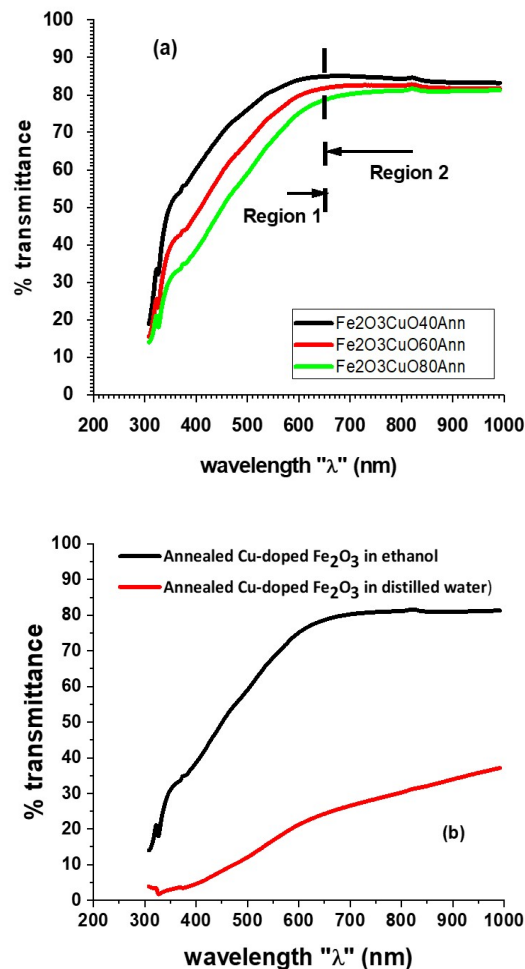


Figure 3: (a) Effect of the number of passes on the transmittance of Cu-doped Fe₂O₃ and (b) comparison of the effect of precursor solvent on the transmittance for 80 passes.

the matrix elements of optical transitions which is assumed to be independent of energy, E_g is the Tauc's optical gap and B depends on the material composition and deposition method and conditions, m is the order of transition that take values of 1/2, 2, 3/2 and 3 representing direct allowed, indirect allowed, direct forbidden and indirect forbidden transitions, respectively.

Other approximations such as the Absorption Fitting Spectrum (AFS) procedure and David-Mott model exist for determining the band gap of semiconducting materials. Absorption Fitting Spectrum [74] uses equation (3) but is expressed

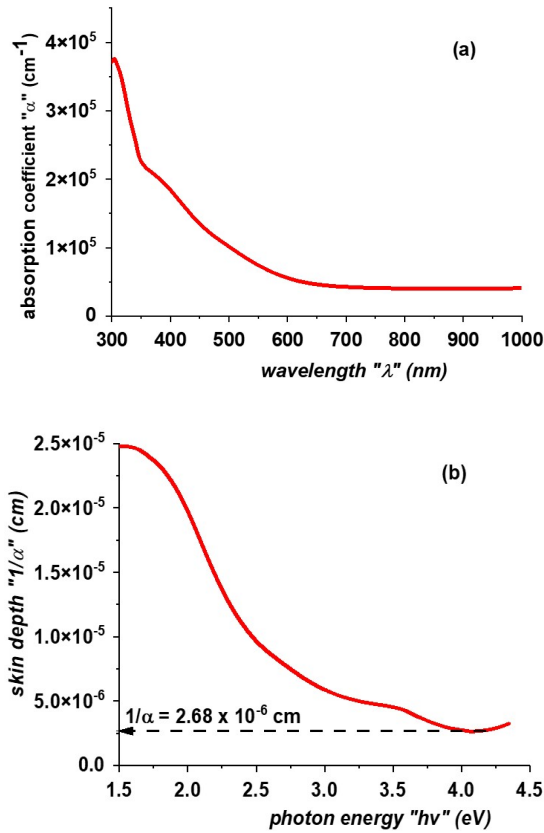


Figure 4: Graphical representation of the variation of (a) the absorption coefficient with wavelength and (b) the skin depth with photon energy for Cu-doped Fe_2O_3 from ethanol solution.

in terms of “ λ ”. Rearranging equation (3) gives

$$\frac{\alpha hc}{\lambda} = B \left(\frac{hc}{\lambda} - \frac{hc}{\lambda_g} \right)^m \quad (4)$$

where for direct transition ($m = 1/2$) and indirect transition ($m = 2$), we obtain

$$\left(\frac{\alpha}{\lambda} \right)^2 = K \left(\frac{1}{\lambda} - \frac{1}{\lambda_g} \right) \text{ and } \left(\frac{\alpha}{\lambda} \right)^{\frac{1}{2}} = C \left(\frac{1}{\lambda} - \frac{1}{\lambda_g} \right) \quad (5)$$

where λ_g , h , and c are the wavelength corresponding to the optical bandgap value, Planck’s constant, and the velocity of light respectively. Davis and Mott on the other hand proved that through the in-depth analysis of the matrix elements for transitions between extended states and those between weakly localized states, the absorption coefficient (α) can be expressed through the following equation [75–77]

$$\alpha hv = \frac{4\pi\sigma_{\min}}{3\pi c (\Delta E)^2} (hv - E_2)^3. \quad (6)$$

This can be re-written as:

$$(\alpha hv)^{\frac{1}{3}} = K (hv - E_2), \quad (7)$$

where $\sigma_{\min} = \left(\frac{2\pi^3 c^2 h^3 a}{m^2} \right) [N(E_c)]^2$ is the minimum metallic conductivity and $E_2 = E_c - E_v$. Thus plotting $(\alpha hv)^m$ against

hv for Tauc approximation, $\left(\frac{\alpha}{\lambda} \right)^m$ against $\frac{1}{\lambda}$ for AFS procedure and $(\alpha hv)^m$ against hv for Davis-Mott model where $m = 1/2$ or 2 for direct and indirect electronic transitions in the case of Tauc and AFS but $m = 1/3$ or $2/3$ for direct and indirect transitions in the case of Davis-Mott, which actually represent direct forbidden and indirect forbidden transitions respectively, we obtain Figure 3.

Graphical representation of equations (3), (5) and (7) for determining the bandgap is depicted in Figure 3 (a-c) and the result is presented in Table 3. It can be observed that for direct electronic transition, the three models gave almost equal values of 3.11, 3.44, and 3.43 eV while for indirect electronic transition the disparity in the values is wide, 3.44, 1.98, and 2.32 eV. Since it is a known fact that the direct band gap energy is always higher than an indirect band gap energy, the Davis-Mott model does not reflect this trend and therefore can be neglected. On the other hand, AFS and Tauc models follow this trend and can lead us to say that Cu-doped Fe_2O_3 has an indirect bandgap that lies between 1.98 and 2.32 eV and a direct band gap of 3.43 eV. This can be explained by noting that the initial orbital assignments of the bandgap suggested it was due to an indirect transition of Fe^{3+} d–d origin and that a stronger direct transition involving a charge transfer from an $\text{O}2p$ orbital to $\text{Fe}3d$ did not occur until 3.2 eV [11]. The result indicates that Fe_2O_3 prepared through ethanol solution is an indirect band gap material though many researchers concluded that Cu-doped Fe_2O_3 can exhibit both a direct and an indirect bandgap transition [10–15].

Table 3: Analyses of the different models employed in determining the band gap of Cu-doped Fe_2O_3 film.

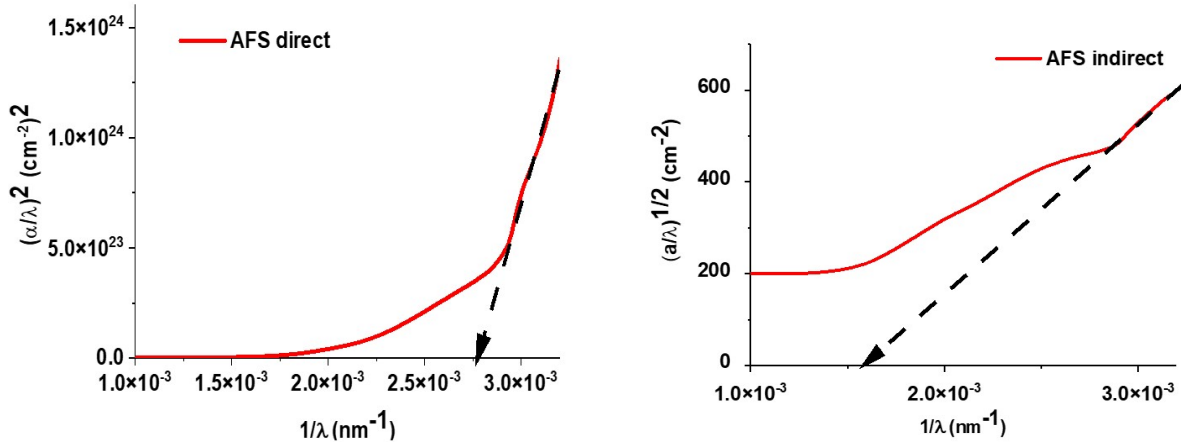
Model	Direct (eV)	Indirect (eV)
Davis-Mott	3.11	3.44
AFS	3.44	1.98
Tauc	3.43	2.32

3.4.4. Urbach band tail energy

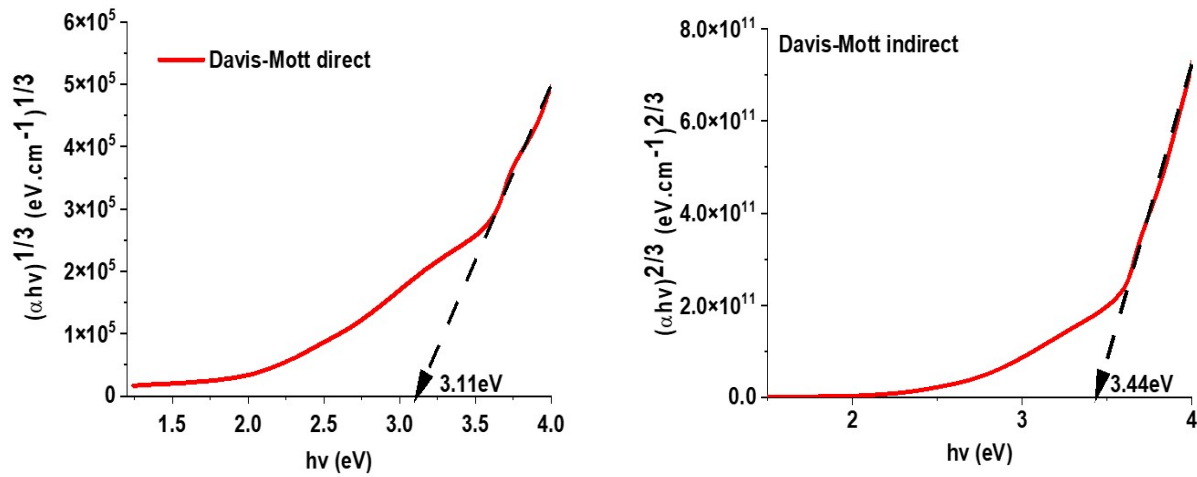
At photon energies below the exponential absorption edge, there is a sub-gap absorption that originates from transitions between deep localized electron states in the pseudo-gap and extended states in the conduction and the valence bands. The exponential rise is called the Urbach tail and it appears in polycrystalline, partially crystalline, and non-crystalline materials, because of the existence of these localized states [78–80]. The relationship between the absorption coefficient and Urbach tail energy is given as

$$\alpha = \alpha_o e^{\frac{hv}{E_U}}, \quad (8)$$

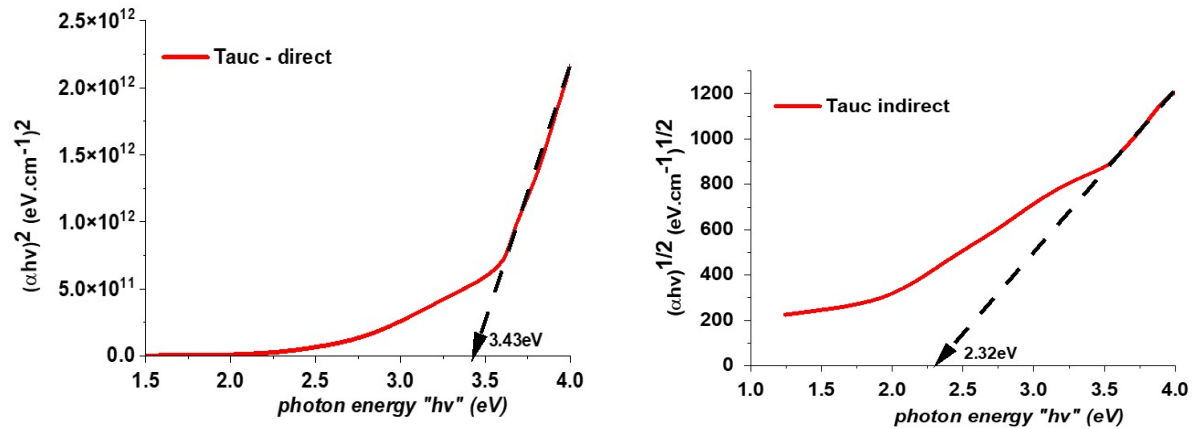
where α_o is a constant and E_U refers to the energy of the band-tail width (Urbach energy). This energy, E_U depends slightly on temperature and is often interpreted as the band-tail width owing to the localized states in the forbidden band gap and associated with the perturbation of the non-crystalline and low crystalline materials [81]. Linearisation of equation (8) and



(a) Band gap determination using AFS model for direct (left) and indirect (right) transition.



(b) Band gap determination using Davis-Mott model for direct (left) and indirect (right) transition.



(c) Band gap determination using Tauc's method for direct (left) and indirect (right) transition.

Figure 5: Band gap determination

plotting $\ln \alpha$ against $h\nu$ gives a straight line where the inverse of the slope is the value of Urbach energy.

$$\ln \alpha = \ln \alpha_o + \frac{h\nu}{E_U} \tag{9}$$

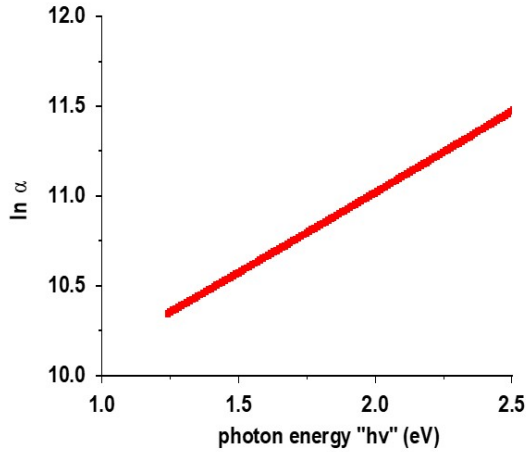


Figure 6: Plot of $\ln \alpha$ against $h\nu$ for Urbach energy determination

The plot of $\ln \alpha$ against $h\nu$ is presented in Figure 6 where the straight line nature is observed. The value calculated for Urbach energy from the slope is 1,100 meV. The Urbach energy quantifies the steepness of the onset of absorption near the band edge, and hence the broadness of the density of states. Since a sharper onset of absorption represents a lower Urbach energy, Cu-doped Fe₂O₃ has a broad onset of absorption.

3.4.5. Steepness Parameter

There is another expression that relates the absorption coefficient α to the band gap energy E_g according to Urbach's assumption [67–69] given by

$$\alpha = \beta \exp \left[\frac{\sigma(h\nu - E_o)}{k_B T} \right], \quad (10)$$

where β is a pre-exponential factor, K_B is the Boltzman's constant, T is the temperature, σ is another optical constant called the steepness parameter, E_o is the energy of the transition which depends on the type of transition. If it is a direct transition, $E_o = E_g$ while for indirect transition $E_o = E_g \pm E_{ph}$ where E_{ph} is the energy due to lattice vibration. Since we have agreed that this is a direct transition then we can replace E_o with E_g in equation (10). Simplifying the equation by taking the natural logarithm of both sides gives

$$\begin{aligned} \ln \alpha &= \ln \beta + \frac{\sigma h\nu}{K_B T} - \frac{\sigma E_g}{K_B T} \\ \ln \alpha &= \left(\ln \beta - \frac{\sigma E_g}{K_B T} \right) + \frac{\sigma h\nu}{K_B T} \end{aligned} \quad (11)$$

We then obtain

$$\ln \alpha_o = \left[\ln \beta - \frac{\sigma E_g}{K_B T} \right] \text{ and } \frac{h\nu}{E_U} = \frac{\sigma h\nu}{K_B T} \quad (12)$$

$$\Rightarrow \sigma = \frac{K_B T}{E_U} \quad (13)$$

where $K_B = 8.6173 \times 10^{-5} \text{ eV.K}^{-1}$ and $T = 300 \text{ K}$ (room temperature). Therefore, we can calculate the steepness parameter σ for Cu-doped Fe₂O₃ to be 7.83 and the electron-phonon coupling energy, $E_{ph} = \frac{2}{3\sigma}$ to be 0.85 eV while $\alpha_o = 1.03 \times 10^4 \text{ cm}^{-1}$.

4. Refractive index, reflectance and extinction coefficient

The refractive index which governs the speed of wave propagation, reflectance which indicates the percentage of the wave reflected and the extinction coefficient which shows the propagation loss in a material are important parameters in determining the optical properties of thin films to be employed in optoelectronic devices. In the present study, the reflectance had been determined using the relation:

$$R = 1 + \left[T e^{2.303\alpha t} \right]^{\frac{1}{2}}, \quad (14)$$

where T is the transmittance, α is the absorption coefficient, and t is the film thickness obtained from the RBS study. The refractive index n , the extinction coefficient k and the optical conductivity σ were determined through equations (15) and (16).

$$n = \frac{1 + \sqrt{R}}{1 - \sqrt{R}} \quad (15)$$

$$k = \frac{\alpha \lambda}{4\pi} \quad (16)$$

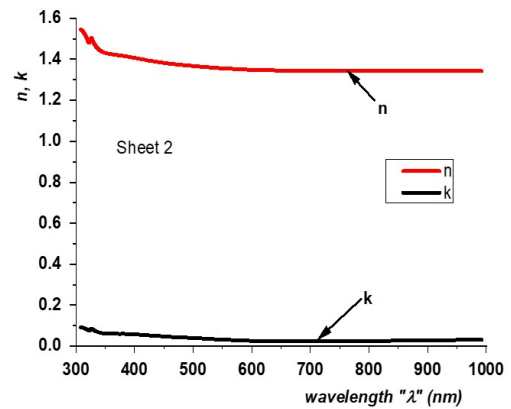


Figure 7: Plot of n and k against wavelength for Cu-doped Fe₂O₃

Graphical representation of equations (15) and (16) against wavelength is shown in Figure 7 to understand their variations as photon energy changes. The refractive index showed a high value at high energy and decreased as the wavelength increased and became constant from 700 nm. The extinction coefficient also showed the same trend as the refractive index. Both “ n ” and “ k ” became constant from 700 nm up to 1000 nm. The figure also indicated that the refractive index is 16 times higher than the extinction coefficient. The dependence of the index of refraction on photon energy can be well described using

a single-effective-oscillator formulation according to Wemple and Di-Domenico [82, 83]

$$n^2 - 1 = \frac{E_d E_{osc}}{E_{osc}^2 - (h\nu)^2} \quad (17)$$

By taking the inverse of equation (17), we obtain

$$\frac{1}{(n^2 - 1)} = \frac{E_{osc}}{E_d} - \frac{(h\nu)^2}{E_d E_{osc}}, \quad (18)$$

where E_{osc} is the single-oscillator energy and E_d is the dispersion energy. By plotting $(n^2 - 1)^{-1}$ against $(h\nu)^2$ we obtain a straight line whose intercept equals $\frac{E_{osc}}{E_d}$ and the slope is $\frac{1}{E_d E_{osc}}$. The graph is presented in Figure 8 where the values of 4.44 and 6.12 eV were obtained for E_d and E_{osc} respectively. The expression (17) holds for photon energies well below E_{osc} . At energies approaching E_{osc} , deviations to the simple law originating from the proximity of the main band-to-band transitions, are measured.

Furthermore, the knowledge of E_d and E_{osc} can be utilized in determining the zero-frequency dielectric constant ϵ_o and zero frequency refractive index n_o through the relation (19), and the values obtained are recorded in Table 4.

$$\epsilon_o = n_o^2 = 1 + \frac{E_d}{E_{osc}} \quad (19)$$

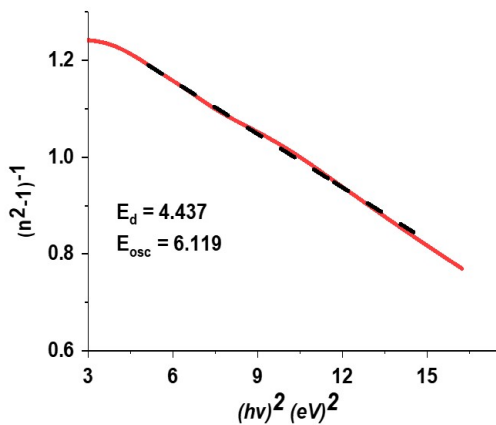


Figure 8: Plot for the determination of the single oscillator energy (E_{osc}) and the dispersion energy (E_d)

Another way of discussing the dispersion parameters is to employ the long wavelength approximation of the single-term Sellmier relation since it retains the physical significance of the oscillator parameters. The relation is given by equation (19),

$$n^2 - 1 = \frac{S_o \lambda_o^2}{1 - \left(\frac{\lambda_o}{\lambda}\right)^2}, \quad (20)$$

where S_o is the average oscillator strength and λ_o is the average oscillator parameter. Again, linearising equation (20) gives,

$$(n^2 - 1)^{-1} = \frac{1}{S_o \lambda_o^2} - \frac{1}{\lambda^2 S_o}. \quad (21)$$

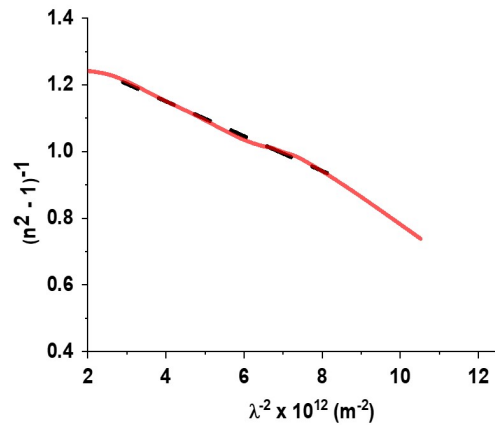


Figure 9: Graph for determining the average oscillator strength (S_o) and average oscillator parameter (λ_o).

Plotting $(n^2 - 1)^{-1}$ against λ^{-2} will give a straight line whose intercept $\left(\frac{1}{S_o \lambda_o^2}\right)$ and the slope is $\left(\frac{1}{S_o}\right)$ can be determined and the graph is presented in Figure 9. The dispersion parameter $\frac{E_o}{S_o}$ where $E_o = \frac{hc}{e\lambda_o}$ can also be determined. The values of S_o , λ_o and $\frac{E_o}{S_o}$ determined through this process is tabulated in Table 4.

4.1. Density of State Effective Mass Ratio

The relationship between the refractive index “n” and the wavelength of the incident photon can also be employed to determine the density of state effective mass ratio and the high frequency dielectric constant through equation (22):

$$n^2 = \epsilon_\infty - \frac{1}{4\pi^2 \epsilon_o} \left(\frac{e^2}{c^2}\right) \left(\frac{N_c}{m^*}\right) \lambda^2 \quad (22)$$

where ϵ_∞ is the high frequency dielectric constant, “e” is the electronic charge, “c” is the speed of light and “ N_c/m^* ” is the density of state effective mass ratio. Plotting n^2 against λ^2 will give a curve where the intercept of the straight part of the curve on the y-axis equals ϵ_∞ and $\left(\frac{N_c}{m^*}\right)$ can be determined from the slope which is $\frac{1}{4\pi^2 \epsilon_o} \left(\frac{e^2}{c^2}\right) \left(\frac{N_c}{m^*}\right)$. With $m^* = 0.44 m_o$, the value of N_c can also be calculated. These values of ϵ_∞ , N_c/m^* and N_c are recorded in Table 4.

4.2. Dielectric constant

The knowledge of “n” and “k” permits the determination of the real, imaginary, and loss tangent of Cu-doped Fe_2O_3 films through equations (23)-(25), and the graphical representation is depicted in Figure 11.

$$\epsilon_r = n^2 - k^2 \quad (23)$$

$$\epsilon_i = 2nk \quad (24)$$

$$\tan \delta = \frac{\epsilon_i}{\epsilon_r} \quad (25)$$

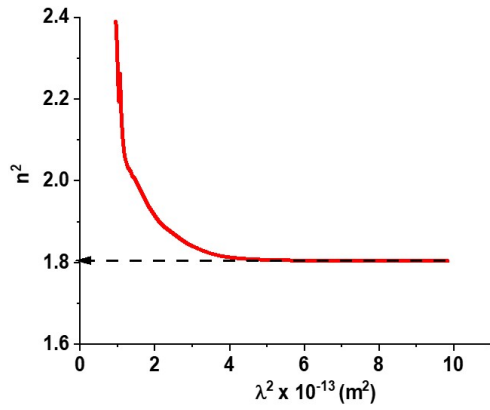


Figure 10: Variation of n^2 vs λ^2 for the determination of the high frequency dielectric constant ϵ_∞ and the density of state N_c

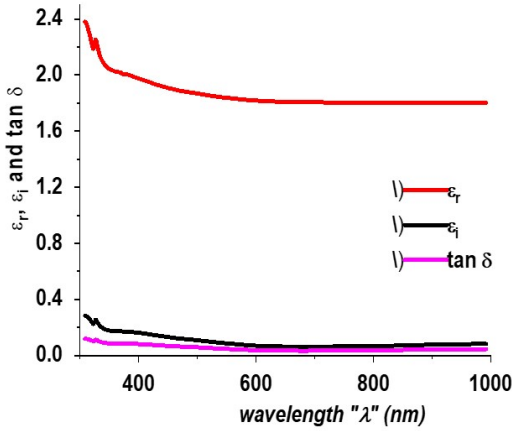


Figure 11: Variation of ϵ_r , ϵ_i and $\tan \delta$ with photon wavelength

Figure 11 shows that ϵ_r is far greater than ϵ_i since ϵ_i is a product of n and k and with smaller values of k , ϵ_i will be lower than ϵ_r . It can also be observed that ϵ_r , ϵ_i and $\tan \delta$ decreased gradually until around 700 nm where they become independent of the photon wavelength. The variation of these three parameters is an indication of photon energy interaction with the free electrons of the Cu-Fe₂O₃ matrix. The low loss tangent ($\tan \delta$) means that energy dissipation and propagation loss of the photons in the matrix are low indicating that photons are able to pass freely in the matrix which will lead to increased optical mobility and conductivity.

4.3. Relaxation time, mobility, resistivity and conductivity

The variation of the imaginary part of the dielectric constant ϵ_i with wavelength can also be employed to determine the relaxation time τ , optical mobility " μ_{opt} ", optical resistivity " ρ_{opt} " and optical conductivity " σ_{opt} " through the following equations:

$$\epsilon_i = \frac{1}{4\pi^3 \epsilon_0} \left(\frac{e^2}{c^3} \right) \left(\frac{N_c}{m^*} \right) \cdot \frac{1}{\tau} \lambda^3 \quad (26)$$

Table 4: Elemental composition, optical, dielectric and oscillator parameters for Cu-doped Fe₂O₃

Parameter	Symbol & Unit	Cu doped Fe ₂ O ₃
Iron content	Fe (at. %)	39.35
Oxygen content	O2 (at. %)	59.62
Copper content (at. %)	Cu (at. %)	1.03
Plasma frequency	ω_p (s ⁻¹)	6.85×10^{13}
High frequency dielectric constant	ϵ_∞	1.81
Film thickness	t (nm)	51.77
Density of state effective mass ratio	N_c/m^* (m ⁻³ .kg ⁻¹)	5.1×10^{54}
Optical carrier charge density	N_c (m ⁻³)	2.0×10^{24}
Urbach energy	E_u (meV)	1,100
Relaxation time	τ (s)	1.3×10^{-14}
Optical mobility	μ (m ² .V ⁻¹ .s ⁻¹)	5.2×10^{-3}
Optical resistivity	ρ (Ω .m)	6.0×10^{-4}
Optical conductivity	σ (Ω^{-1} m ⁻¹)	1.67×10^3
Effective single oscillator energy	E_{osc} (eV)	6.12
Dispersion energy	E_d (eV)	4.44
Effective single oscillator energy band gap ratio	E_{osc}/E_g	2.64 - 3.09
Zero frequency refractive index	n_0	1.31
Zero frequency dielectric constant	ϵ_0	1.72
Average oscillator strength	S_{osc} (m ⁻²)	1.93×10^{13}
Average oscillator wavelength	λ_{osc} (m)	1.95×10^{-7}
Average oscillator energy	E_0 (eV)	6.33×10^{18}
Dispersion parameter	E_0/S_0 (eV.m ²)	3.30×10^5
Bandgap	E_g (eV)	1.98 – 2.32
Linear susceptibility	$\chi^{(1)}$	5.8×10^{-2}
Nonlinear susceptibility	$\chi^{(3)}$ (esu)	1.79×10^{-15}
Nonlinear refractive index	n_2 (esu)	5.1×10^{-14}

$$\mu_{opt} = \frac{e\tau}{m^*} \quad (27)$$

$$\rho_{opt} = \frac{1}{e\mu_{opt}N_c} \quad (28)$$

$$\sigma_{opt} = \frac{1}{\rho_{opt}} \quad (29)$$

where "e", "c" and "m*" are the electronic charge, velocity of light and effective mass (0.44 m_0) of free charge carriers respectively. The plot of ϵ_i against λ^3 will produce a curve where the slope of the linear part of the curve equals $\frac{1}{4\pi^3 \epsilon_0} \left(\frac{e^2}{c^3} \right) \left(\frac{N_c}{m^*} \right) \cdot \frac{1}{\tau}$ which gave τ to be equal to 1.3×10^{-14} s. With this value of τ ,

μ_{opt} , ρ_{opt} and σ_{opt} are determined as tabulated in Table 4. The values obtained from this study are of the same order of magnitude with the values obtained for some chalcogenide compounds [84].

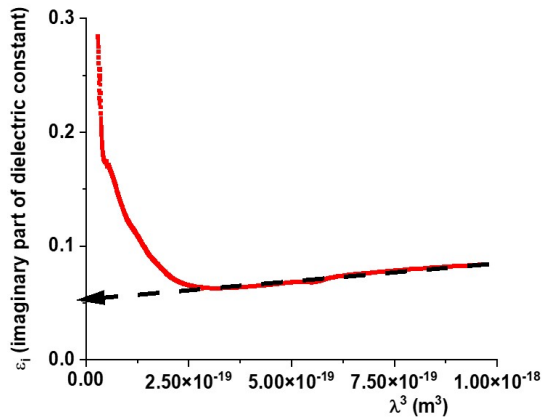


Figure 12: Plot of ϵ_i versus λ^3 for the determination of the relaxation time.

4.4. Plasma Frequency

The relationship between n^2 and λ^2 given in equation (22) can also be expressed in another form:

$$n^2 = \epsilon_{\infty} - \left(\frac{w_p^2}{4\pi c^2} \right) \lambda^2. \quad (30)$$

Comparing equation (23) with (30), it can be seen that both equations have the same slope and with the slope of equation (22) determined to be 4.16×10^9 and equating this value to $\left(\frac{w_p^2}{4\pi c^2} \right)$ which is the slope of equation (30), the value of w_p has been calculated to be $6.85 \times 10^{13} \text{ s}^{-1}$. This value corresponds well with the values obtained by other authors [84].

4.5. Optical nonlinearity

Nonlinear optic happens in a media where the polarization density P responds non-linearly to the electric field E of the light. The non-linearity is typically observed only at very high light intensities. Nonlinear optical phenomena, in which the optical fields are not too large, can be described by a Taylor series expansion of the dielectric polarization density (electric dipole moment per unit volume) $P(t)$ at time t in terms of the electric field $E(t)$:

$$P(t) = \epsilon_o \left(\chi^{(1)} E(t) + \chi^{(2)} E^2(t) + \chi^{(3)} E^3(t) + \dots \right) \quad (31)$$

where the coefficients $\chi^{(n)}$ are the n-th-order susceptibilities of the medium, and the presence of such a term is generally referred to as an n-th-order nonlinearity. Simple semiempirical relation based on generalized Miller's rule allows an estimation of nonlinear susceptibility ($\chi^{(3)}$) and non-linear refractive index (n^2) from linear refractive index and/or from the dispersion energy and the energy of effective oscillator of the Wemple-Di

Domenico model [84, 85]. The relevant equations are expressed below:

$$\chi^{(1)} = \frac{E_d}{4\pi E_{so}} \quad (32)$$

$$\chi^{(3)} = C \left[\left(\frac{n_o^2 - 1}{4\pi} \right)^4 \right] \quad (33)$$

$$n_2 = \frac{12\pi\chi^{(3)}}{n_o} \quad (34)$$

where $\chi^{(1)}$, $\chi^{(3)}$, n_o and C are the linear susceptibility, nonlinear susceptibility, nonlinear refractive index and a constant which is equal for all materials with a value of 1.7×10^{-10} esu and it is independent of frequency. The values obtained using equations (32)-(34) are tabulated in Table 4.

5. Conclusion

Cu-doped hematite thin films were prepared from a mixture of distilled water and ethanol precursor using spray pyrolysis technique. Apart from RBS studies that provided the film thickness and the composition, all other parameters of the films were deduced from the optical transmittance studies. RBS showed that only the Cu-doped film prepared from ethanol solution gave the composition very close to Fe_2O_3 with film thickness of 51.77nm. Optical transmittance studies of the Cu-doped films also showed that the transmittance of the film prepared using distilled water is lower than that of ethanol solution which is an indication that ethanol solution produced nano-thick films of high integrity. Cu-doped Fe_2O_3 film is highly absorbing with α greater than 10^5 cm^{-1} . Tauc, AFS and Davis and Mott models were employed to determine the actual value of the bandgap using direct and indirect transition to conclude that Cu-doped Fe_2O_3 is an indirect bandgap material with $1.98 \text{ eV} < E_g < 2.32 \text{ eV}$ and a direct band gap energy of 3.43 eV. The value of Urbach energy gave an indication of a broad onset of absorption. The variations of the refractive index with photon energy or wavelength allowed the estimation of the single-oscillator energy, dispersion energy, average oscillator strength, average oscillator parameter, dispersion parameter, density of state effective mass ratio, high frequency dielectric constant and the plasma frequency. $\epsilon_{\infty} > n_o^2$ means that free charge carriers contribute in the polarization process within Cu-doped Fe_2O_3 thin film. The variation of the imaginary part of the dielectric constant (ϵ_i) with photon wavelength led to the estimation of the relaxation time, optical mobility, resistivity and optical conductivity. The 1st and 3rd order nonlinear susceptibility and nonlinear refractive index were estimated. All the values of the parameters estimated were of the same order of magnitude with other semiconducting materials. The values also indicated that Cu-doped Fe_2O_3 film could be suitable for nonlinear, electrochemical as well as optoelectronic applications.

References

- [1] Y. Zhu, H. Lu, Y. Lu & X. Pan, "Characterization of SnO₂ Films Deposited by D.C. Gas Discharge Activating Reaction Evaporation onto Amorphous and Crystalline-substrates", *Thin Solid Films* **224** (1993) 82.
- [2] C. C. Chai, J. Peng & B. P. Yan, "Preparation and Gas-Sensing Properties of α -Fe₂O₃ thin Films", *Journal of Electronic Materials* **24** (1995) 799.
- [3] M. Chen, G. Diao & X. Zhou, "Nanotechnology" **18** (2007) 275606.
- [4] R. N. Goyal, D. Kaur & A. K. Pandey, "Growth and characterization of iron oxide nanocrystalline thin films via low-cost ultrasonic spray pyrolysis", *Materials Chemistry and Physics* **116** (2009) 638.
- [5] M. Ritu, "A Simple and Effective Method of the Synthesis of Nanosized Fe₂O₃ particles", *IOSR Journal of Applied Chemistry* **4** (2013) 41.
- [6] M. Aronniemi, J. Lahtinen & P. Hautiojarvi, "Characterization of iron oxide thin films", *Surf. Interface Anal.* **36** (2004) 1004.
- [7] Z. Hubicka, S. Kment, J. Olejníček, M. Cada, T. Kubart, M. Brunclik, P. Ksirov, P. Adámek & Z. Remes, "Deposition of hematite Fe₂O₃ thin film by DC pulsed magnetron and DC pulsed hollow cathode sputtering system", *Thin Solid Films* **549** (2013) 184.
- [8] SPRINGER Encyclopedia of Soil Science, Edited by Chesworth W. **XXVI** (2008) 369.
- [9] F.H. Fermin, D. Aragon, J. Ardisson, Juan C.R. Aquino, I. Gonzalez, W. A. Macedo, A.H. Coaquira, J. Mantilla, S. W. da Silva, & P. C. Morais, "Effect of the thickness reduction on the structural, surface and magnetic properties of α -Fe₂O₃ thin films", *Thin Solid Films* **607** (2016) 54.
- [10] M. R. Belkhedkar, & A. U. Ubale, "Preparation and Characterization of Nanocrystalline α -Fe₂O₃ Thin Films Grown by Successive Ionic Layer Adsorption and Reaction Method", *International Journal of Materials and Chemistry* **4** (2014) 109.
- [11] L. A. Marusak, R. Messier, W. B. White, *J. Phys. Chem. Solids* **41** (1980) 981.
- [12] N. Beermann, L. Vayssieres, S. E. Lindquist & A. Hagfeldt, *J. Electrochem. Soc.* **147** (2000) 2456.
- [13] A. Kleiman-Shwarstein, Y. S. Hu, A. J. Forman, G. D. Stucky, & E. W. McFarland, *J. Phys. Chem. C* **112** (2008) 15900.
- [14] N. C. Debnath, A. B. Anderson, *J. Electrochem. Soc.* **129** (1982) 2169.
- [15] K. Sivula, F. Le Formal, & M. Gratzel, "Solar Water Splitting: Progress Using Hematite (α -Fe₂O₃) Photoelectrodes", *ChemSusChem* **4** (2011) 432.
- [16] R. N. Goyal, D. Kaur, & A. K. Pandey, "Growth and characterization of iron oxide nanocrystalline thin films via low-cost ultrasonic spray pyrolysis", *Materials Chemistry and Physics* **116** (2009) 638.
- [17] M. Mishra & D.-M. Chun, " α -Fe₂O₃ as a Photocatalytic material: A Review", *Applied Catalysis A, General* (2015) 023.
- [18] Z. Zhou, Q. Zhang, J. Sun, B. He, J. Guo, Q., Li, C. Li, L. Xie, & Yangang Yao, "Metal-Organic Framework Derived Spindle-like Carbon Incorporated α -Fe₂O₃ Grown on Carbon Nanotube Fiber as Anodes for High-Performance Wearable Asymmetric Supercapacitors", *ACS Nano* **12** (2018) 9333.
- [19] S. Gahlawata, N. Rashida & P. P. Ingole, "n-Type Cu₂O/ α -Fe₂O₃ Heterojunctions by Electrochemical Deposition: Tuning of Cu₂O Thickness for Maximum Photoelectrochemical Performance", *Z. Phys. Chem.* **232** (2018) 1551.
- [20] H. Magan, D. Stanescu, M. Rioult, E. Fonda, & A. Barbier, Enhanced photoanode properties of epitaxial Ti doped α -Fe₂O₃ (0001) thin films, *Applied Physics Letters* **101** 133908 (2012).
- [21] L. Wang, C-Y. Lee, A. Mazare, K. Lee, J. Muller, E. Spiecker & P. Schmuki, "Enhancing the Water Splitting Efficiency of Sn-Doped Hematite Nanoflakes by Flame Annealing", *Chem. Eur. J.* **20** (2014) 88.
- [22] A. Annamalai, P. S. Shinde, T. H. Jeon, H. H. Lee, H. G. Kim, W. Choi & J. S. Jang, "Fabrication of superior α -Fe₂O₃ nanorod photoanodes through ex-situ Sn-doping for solar water splitting", *Solar Energy Materials & Solar Cells* **144** (2016) 247.
- [23] I. Cesar, K. Sivula, A. Kay, R. Zboril & M. Gratzel, "Influence of Feature Size, Film Thickness, and Silicon Doping on the Performance of Nanostructured Hematite Photoanodes for Solar Water Splitting", *J. Phys. Chem. C* **113** (2009) 772.
- [24] P. Sharma, P. Kumar, D. Deva, R. Shrivastav, S. Dass & V. R. Satsangi, "Nanostructured Zn-Fe₂O₃ thin film modified by Fe-TiO₂ for photoelectrochemical generation of hydrogen", *International Journal of Hydrogen Energy* **35** (2010) 10883.
- [25] C. Jorand Sartoretti, M. Ulmann, B.D. Alexander, J. Augustynski & A. Weidenkaff, "Photoelectrochemical oxidation of water at transparent ferric oxide film electrodes", *Chemical Physics Letters* **376** (2003) 194.
- [26] I. K. Kim, Y. G. Kim & T. Y. Park, "Preparation and Characterization on Thin Films of Doped Iron Oxide Semiconductive Electrodes", *Analytical Sciences* **7** (1991) 222.
- [27] S. Krehula, G. Stefanic, K. Zadro, L. K. Krehula, M. Marcius, S. Music, "Synthesis and properties of iridium-doped hematite (α -Fe₂O₃)", *Journal of Alloys and Compounds* **545** (2012) 200.
- [28] L. Wang, C-Y Lee & P. Schmuki, "Ti and Sn co-doped anodic α -Fe₂O₃ films for efficient water splitting", *Electrochemistry Communications* **30** (2013) 21.
- [29] C. X. Kronawitter, I. Zegkinoglou, S.-H. Shen, P. Liao, I. S. Cho, O. Zandi, Y.-S. Liu, K. Lashgari, G. Westin, J.-H. Guo, F. J. Himpel, E. A. Carter, X. L. Zheng, T. W. Hamann, B. E. Koel, S. S. Mao & L. Vayssieres, "Titanium incorporation into hematite photoelectrodes: theoretical considerations and experimental observations", *Energy Environ. Sci.* **7** (2014) 3100.
- [30] C-Y Lee, L. Wang, Y. Kado, R. Kirchgeorg & P. Schmuki, "Si-doped Fe₂O₃ nanotubular/nanoporous layers for enhanced photoelectrochemical water splitting", *Electrochemistry Communications* **34** (2013) 308.
- [31] P. Kumar, P. Sharma, R. Shrivastav, S. Dass & V. R. Satsangi, "Electrodeposited zirconium-doped α -Fe₂O₃ thin film for photoelectrochemical water splitting", *International Journal of Hydrogen Energy* **36** (2011) 2777.
- [32] E. L. Tsege, T. Sh. Atabaev, M. A. Hossain, D. Lee, H-K. Kim & Y-H. Hwang, "Cu-doped flower-like hematite nanostructures for efficient water splitting application", *Journal of Physics and Chemistry of Solids* **98** (2016) 283.
- [33] V. R. Satsangi, S. Kumaria, A. P. Singh, R. Shrivastav & S. Dass, "Nanostructured hematite for photoelectrochemical generation of hydrogen", *International Journal of Hydrogen Energy* **33** (2008) 312.
- [34] Vibha R. Satsangi, Saroj Kumari, A. P. Singh, R. Shrivastav & S. Dass, "Nanostructured hematite for photoelectrochemical generation of hydrogen", *International Journal of Hydrogen Energy* **33** (2008) 318.
- [35] V. Martis, R. Oldman, R. Anderson, M. Fowles, T. Hyde, R. Smith, S. Nikitenko, W. Bras & G. Sankar, "Structure and speciation of chromium ions in chromium doped Fe₂O₃ catalysts", *Phys. Chem. Chem. Phys.* **15** (2013) 168.
- [36] K. V. Siva & R. N. Bhowmik, "Structural, magnetic and magneto-electric properties of Cr doped α -Fe₂O₃", *AIP Conference Proceedings* **2115** (2019) 030491.
- [37] G. Goyal, A. Dogra, S. Rayaprol, S.D. Kaushik, V. Siruguri, H. Kishan, "Structural and magnetization studies on nanoparticles of Nd doped Fe₂O₃", *Materials Chemistry and Physics* **134** (2012) 133.
- [38] I. Kuryliszyn-Kudelskaa, B. Hadzicb, D. Siberac, L. Kilanskia, N. Romcevicb, M. Romcevicb, U. Narkiewicz and W. Dobrowolskia, "Nanocrystalline ZnO Doped with Fe₂O₃ — Magnetic and Structural Properties", *Acta Physica Polonica A* **119** (2011) 689.
- [39] F. S. Freyria, G. Barrera, P. Tiberto, E. Belluso, D. Levy, G. Saracco, P. Allia, E. Garrone, B. Bonelli, "Eu-doped α -Fe₂O₃ nanoparticles with modified magnetic properties", *Journal of Solid State Chemistry* **201** (2013) 311.
- [40] Z., P. Wand, N., Hu, W., S. Kormarmeni, "Anode electrodeposition of 3D mesoporous Fe₂O₃ nonosheets on carbon fabric for flexible solid state asymmetric supercapacitor". *Ceramics international* **45** (2019) 10420.
- [41] V.D. Nithya, N. Sabari Arul, "Review on α -Fe₂O₃ based negative electrode for high performance supercapacitors", *Journal of Power Sources* **327** (2016) 297.
- [42] K. Tang, H. Ma, Y. Tian, Z. Liu, H. Jin, S. Hou, K. Zhou, X. Tian, "3D printed hybrid-dimensional electrodes for flexible micro-supercapacitors with superior electrochemical behaviours", *Virtual and Physical Prototyping* **15** (2020) 511.
- [43] Y-J. Gu, W. Wen, S. Zheng, J-M. Wu, "Rapid synthesis of high-area-capacitance ultrathin hexagon Fe₂O₃ nanoplates on carbon cloth via a versatile molten salt method", *Mater. Chem. Front.* **4** (2020) 2744.
- [44] F. Han, J. Xu, J. Zhou, J. Tang, W. Tang, "Oxygen vacancy-engineered Fe₂O₃ nanoarrays as free-standing electrodes for flexible asymmetric supercapacitors", *Nanoscale* **11** (2019) 12477.
- [45] C. Liu, Q. Li, J. Cao, Q. Zhang, P. Man, Z. Zhou, C. Li, Y. Yao, "Superstructured α -Fe₂O₃ nanorods as novel binder-free anodes for high-

- performing fiber-shaped Ni/Fe battery”, *Science Bulletin* **65** (2020) 812.
- [46] F. Li, Y-L. Liu, G-G. Wang, H-Y. Zhang, B. Zhang, G-Z. Li, Z-P. Wu, “Le-Yang Dang, Jie-Cai Han Few-layered Ti3C2Tx Menes coupled with Fe2O3 nanorod arrays grown on carbon cloth as anodes for flexible asymmetric supercapacitors”, *J. Mater. Chem. A* **7** (2019) 22631.
- [47] Q Wang, C. Guo, J. He, S. Yang, Z. Liu, Q. Wang, “Fe2O3/C-modified Si nanoparticles as anode material for high-performance lithium-ion batteries”, *Journal of Alloys and Compounds* **30** (2019) 284.
- [48] K Le, M. Gao, D. Xu, Z. Wang, G. Wang, W. Liu, F. Wang, J. Liu, “Polypyrrole-coated Fe2O3 nanotubes constructed from nanoneedles as high-performance anodes for aqueous asymmetric supercapacitors”, *Dalton Trans.* **49** (2020) 9709.
- [49] X.-F. Lu, X.-Y. Chen, W. Zhou, Y.-X. Tong, G.-R. Li, “ α -Fe2O3 PANI Core-Shell Nanowire Arrays as Negative Electrodes for Asymmetric Supercapacitors”, *ACS Appl. Mater. Interfaces* **7** (2015) 14850.
- [50] Y. Luo, J. Luo, J. Jiang, W. Zhou, H. Yang, X. Qi, H. Zhang, H. J. Fan, Denis Y. W. Yu, C. M. Li & T. Yu, “Seed-assisted synthesis of highly ordered TiO2@ α -Fe2O3 core/shell arrays on carbon textiles for lithium-ion battery applications”, *Energy Environ. Sci.* **5** (2012) 6566.
- [51] M. Yang, S. Z. Qing, Y. Cuang, G. Wang, S., Teng, Fei, L. Guohua & A. Zhaoqun, “Cu-Doped α -Fe2O3 Microspheres as Anode Materials for Lithium-Ion Batteries”, *Journal of Nanoscience and Nanotechnology* **16** (2018) 4296.
- [52] F. A. Harraz, A. A. Ismail, S. A. Al-Sayari & A. Al-Hajry, “Novel Fe2O3/Polypyrrole Nanocomposite with Enhanced Photocatalytic Performance”, *Journal of Photochemistry and Photobiology A: Chemistry* **299** (2015) 18.
- [53] J-C. Wu, W-M. Yan, C-T. Wang, C-H. Wang, Y-H. Pai, K-C. Wang, Y-M. Chen, T-H. Lan & S. Thangavel, “Treatment of Oily Wastewater by the Optimization of Fe2O3 Calcination Temperatures in Innovative Bio-Electron-Fenton Microbial Fuel Cells”, *Energies* **11** (2018) 565.
- [54] T. K. Singh, S. A. Bansal & S. Kumar, “Graphene oxide (GO)/Copper doped Hematite (α -Fe2O3) nanoparticles for organic pollutants degradation applications at room temperature and neutral pH, *Materials Research Express* **6** (2019) 115026.
- [55] H. Feng, L. Tang, J. Tang, G. Zeng, H. Dong, Y. Deng, L. Wang, Y. Liu, X. Ren & Y. Zhou, “Cu-Doped Fe2O3 core-shell nanoparticle shifted oxygen reduction pathway for high-efficiency arsenic removal in smelting wastewater”, *Environ. Sci.: Nano* **5** (2018) 1595.
- [56] S. S. Chahal, A. Kumar & P. Kumar, “Zn Doped α -Fe2O3: An Efficient Material for UV Driven Photocatalysis and Electrical Conductivity”, *Crystals* **273** (2020) 18.
- [57] S. Upasen, “Activated carbon-doped with iron oxide nanoparticles (α -Fe2O3 NPs) preparation: particle size, shape, and impurity”, *International Journal of ChemTech Research* **11** (2018) 33.
- [58] O.M. Lemine I. Ghiloufi, M. Bououdina, L. Khezami, M. O. M’hamed, A.T. Hassan, “Nanocrystalline Ni-doped α -Fe2O3 for adsorption of metals from aqueous solution”, *Journal of Alloys and Compounds* **588** (2014) 592.
- [59] A. A. Ismail, “Synthesis and characterization of Y2O3/ Fe2O3/TiO2 nanoparticles by sol-gel method”. *Applied Catalysis B: Environmental* **58** (2005) 115.
- [60] J. Ouyang, Z. Zhao, S.L. Sui & H. Yang, “Degradation of Congo Red Dye by a Fe2O3@CeO2-ZrO2/Palygorskite Composite Catalyst: Synergetic Effects of Fe2O3”, *Journal of Colloid and Interface Science* **539** (2019) 135.
- [61] G. Picasso, M.R. Sun Kou, O. Vargasmachuca, J. Rojas, C. Zavala, A. Lopez & S. Irusta, “Sensors based on porous Pd-doped hematite (α -Fe2O3) for LPG detection”, *Microporous and Mesoporous Materials* **185** (2014) 85.
- [62] C. Cantalini, H.T. Sun, M. Faccio, G. Ferri & M. Pelino, “Niobium-doped α -Fe2O3 semiconductor ceramic sensors for the measurement of nitric oxide gases”, *Sensors and Actuators B* **24-25** (1995) 671.
- [63] P. Sun, C. Wang, X. Zhou, P. Cheng, K. Shimanoe, G. Lu, N. Yamazoe, “Cu-doped α -Fe2O3 hierarchical microcubes: Synthesis and gas sensing properties”, *Sensors and Actuators B: Chemical* **193** (2014) 622.
- [64] N. Funazaki, A. Hemmi, S. Ito, Y. Asano, S. Yamashita, T. Kobayashi & M. Haruta, “Development of carbon monoxide detector doped α -Fe2O3”, *Sensors and Actuators B* **13-14** (1993) 538.
- [65] A. M. Schultz, Y. Zhu, S. A. Bojarski, G. S. Rohrer & P. A. Salvador, “Eutaxial growth of hematite Fe2O3 films on perovskite SrTiO3 polycrystalline substrates”, *Thin Solid Films* **548** (2013) 224.
- [66] M. Su, C. He & K. Shih, “Facile synthesis of morphology and size-controlled α -Fe2O3 and Fe3O4 nano- and microstructures by hydrothermal/solvothermal process: The roles of reaction medium and urea dose”, *Ceramics International* **42** (2016) 14793.
- [67] J. A. Glasscock, P. R. F. Barnes, I. C. Plumb, A. Bendavid & P. J. Martin, “Structural, optical and electrical properties of undoped polycrystalline hematite thin films produced using filtered arc deposition”, *Thin Solid Films* **516** (2008) 1716.
- [68] M. N. Batin & V. Popescu, “The influence of deposition time on optical properties of iron oxide films grown on glass substrate by Chemical Bath Deposition”, *Optoelectronics and Advanced Materials – Rapid Communications* **6** (2012) 729.
- [69] A. Lassoued, M. Saber Lassoued, B. Dkhil, A. Gadris & S. Ammar, “Structural, optical and morphological characterization of Cu-doped α -Fe2O3 nanoparticles synthesized through co-precipitation technique”, *Journal of Molecular Structure* **1148** (2017) 281.
- [70] C. Aydin, Sh. A. Mansour, Z. A. Alahmed & F. Yakuphanoglu, “Structural and optical characterization of sol-gel derived boron doped Fe2O3 nanostructured films”, *J. Sol-Gel Sci Technol.* **62** (2012) 397.
- [71] A. Y. Fasasi, E. Osagie, D. Pelemo, E. Obiajunwa, E. Ajenifuja, J. Ajao, G. Osinkolu, W. O. Makinde & A. E. Adeoye, “Effect of Precursor Solvents on the Optical Properties of Copper Oxide Thin Films Deposited Using Spray Pyrolysis for Optoelectronic Applications”, *American Journal of Materials Synthesis and Processing* **3** (2018) 22.
- [72] A.S. Hassanien & A. A. Akl, “Influence of composition on optical and dispersion parameters of thermally evaporated non-crystalline Cd50S50.xSex thin films”, *Journal of Alloys and Compounds* **648** (2015) 290.
- [73] A.S. Hassanien & A. A. Akl, “Effect of Se addition on optical and electrical properties of chalcogenide CdSe thin films”, *Superlattices and Microstructures* **89** (2016) 169.
- [74] J. Tauc & A. Menth, “States in the gap”, *J Non-Crystalline Solids* **8-10** (1972) 585.
- [75] N.F. Mott & E.A. Davis, *Electron processes in non-crystalline materials*, Clarendon, Oxford, 1979.
- [76] E.N. Economou & M. H. Cohen, “Anderson’s theory of localization and the Mott-CFO model”, *Material Research Bulletin* **8** (1970) 590.
- [77] “Optical Properties of Condensed Matter and Applications”, Jai Singh (eds.) Wiley Series in Materials for Electronics and Optoelectronic Applications, John Wiley and Sons Ltd. West Sussex, PO19 8SQ, England, 2006.
- [78] J. Melsheimer & D. Ziegler, Band gap energy and Urbach tail studies of amorphous, partially crystalline and polycrystalline tin dioxide, *Thin Solid Films* **129** (1985) 47.
- [79] S.J. Ikhmayies & R.N. Ahmad-Bitar, “A study of the optical bandgap energy and Urbach tail of spray-deposited CdS:In thin films”, *Journal of Materials Research and Technology* **2** (2013) 227.
- [80] K.A. Aly, A.A. Elnaeim, M. Uosif & O. Abdel-Rahim, “Optical properties of Ge-As-Te thin films”, *Physica B: Condensed Matter* **406** (2011) 4232.
- [81] S. Ikhmayies & R. Ahmad-Bitar, “Thickness dependence of the bandgap energy and Urbach tail for CdS thin films prepared by vacuum evaporation, in: Proceedings of the World renewable energy congress and exhibition **XI** (2010) 979.
- [82] S.H. Wemple & M. Di-Domenico, “Behaviour of the electronic dielectric constant in covalent and ionic materials”, *Phys. Rev. B* **3** (1971) 1350.
- [83] S. H. Wemple, “Refractive-index behaviour of amorphous semiconductors and glasses”, *Phys. Rev. B* **7** (1973) 3776.
- [84] A. S. Hassanien, “Studies on dielectric properties, opto-electrical parameters and electronic polarizability of thermally evaporated amorphous Cd50S50-xSex thin films”, *Journal of Alloys and Compounds* **671** (2016) 578.
- [85] H. Tichá & L. Tichý, “Semiempirical relation between non-linear susceptibility (refractive index), linear refractive index and optical gap and its application to amorphous chalcogenides”, *Journal of Optoelectronics and Advanced Materials* **2** (2002) 386.